Available online at www.sciencedirect.com
ScienceDirect
Trans. Nonferrous Met. Soc. China 35(2025) 2652−2665
Transactions of Nonferrous Metals Society of China
www.tnmsc.cn

Integral casting of Ni-based superalloy melt and Nb-pretreated SiC_f/SiC composite

Guo-biao LIN[1], Fu-hu ZHU[1], Jing-yu LIU[1], Peng LIU[2], Kai-xuan CHEN[1]

1. School of Materials Science and Engineering, University of Science and Technology Beijing, Beijing 100083, China;
2. National Center for Materials Safety Service, University of Science and Technology Beijing, Beijing 100083, China

Received 24 December 2023; accepted 2 July 2024

Abstract: A practical process method for precise integration of SiC_f/SiC composite (CMC) and a Ni-based superalloy (K403) was proposed in this study. It involves Nb coating pretreatment of the CMC via the chemical vapor deposition (CVD) at 1000 °C and subsequent integral precision casting between the pretreated CMC and the K403 superalloy melt. The method solves the difficulty for the dissimilar material to be cast together, forming a robust bonding interface with an average shear strength of 94.8 MPa at room temperature. During the pretreatment process, the Nb reacted with the CMC, forming a reactive coating with the microstructure composed of NbC, Nb_2C and Nb_5Si_3 phases. In the following integral casting, the Nb reactive coating effectively blocked detrimental graphitization reaction between the Ni element in the superalloy melt and the CMC, and mitigated the interface thermal stress generated by both the mismatch of thermal expansion coefficients and temperature difference, resulting in the increase of interfacial strength. The typical interfacial microstructure consists of the CMC, NbC, $NbSi_2$/NbC, SiC, $NbSi_2$, Nb_2C, Nb_5Si_3, Al_4C_3, Nb_2Al/γ/γ' and MC (M=W, Mo, Ti). A formula for estimating the interfacial thermal stress of an integrated cast was derived.

Key words: SiC_f/SiC composite; microstructure; Ni-based superalloy; integral casting; Nb reactive coating; bonding strength

1 Introduction

The SiC_f/SiC composite (SiC fibre-reinforced SiC ceramic matrix composite, CMC) possesses a series of merits, such as low density, outstanding thermo-mechanical properties, excellent chemical stability, and extraordinary resistance to irradiation. Consequently, it has become a preferable high temperature structural material for application in advanced aerospace industry [1−3] and next generation nuclear reactor [3−5]. However, due to its limitations in forming accuracy and toughness as well as its high hardness, it is difficult for the CMC to be processed or machined into a high-precision and complex-shaped component to meet assembly requirements. Therefore, its application involves integration with a metal to utilize its workability, for example, with a nickel-based superalloy to use in turbine aero-engine [6,7]. The introduction of a new method termed “integral casting” through the precision casting of CMC and metal melt presents numerous advantages over conventional methods like brazing and mechanical connection. This approach streamlines fabrication process in which the metal part can be accurately formed by precision casting and simultaneously joined to the CMC part, achieving high assembly accuracy. Additionally, since the metal part is initially in liquid state, the interface between the two parts can be easily made into a proper irregular structure on correct designs [8,9], so that both the interfacial

Corresponding author: Guo-biao LIN, Tel: +86-13146838841, E-mail: lin571@163.com
https://doi.org/10.1016/S1003-6326(25)66838-5

strength and air-tightness can be improved beyond those of a flat interface. Moreover, the absence of low melting point filler required for brazing means that the interfacial high-temperature resistance can easily reach a higher level. Based on the above reasons and the fact that K403 Ni-based superalloy is a remarkable high-temperature resistant structural material used widely in aero-engine, the study on the integral casting of the CMC and K403 superalloy holds great significance for advancing CMC application in the aerospace.

The key to the integral casting is to achieve strong interfacial bonding between the CMC and the superalloy, which is challenging because they are dissimilar materials with different physical and chemical properties, and toughness. But up to now, there have been very few reports on the integral casting of SiC-based material and metal, although substantial effort has been devoted to their brazing connection, including some research [10−14] on the brazing of CMC to Ni-based superalloy. Unlike the brazing, where CMC and a superalloy are joined by molten filler in an isothermal environment with a temperature below the melting point of the superalloy, integral casting involves pouring the superalloy melt at a temperature remarkably higher than that of the heated CMC, resulting in an uneven temperature distribution between the two materials. When the melt touches the CMC, the surface temperature of the CMC will rise sharply, leading to a large temperature gradient in the CMC and consequent thermal shock (referring to the numerical simulation on the casting of SiC ceramic/K4169 alloy [15]), which could potentially cause immediate damage to the CMC. Generally, the CMC has better thermal shock resistance than other ceramics. During the casting process, as the melt flows, fills, penetrates, diffuses, reacts, and cools to room temperature, the interface of the cast evolves into the final microstructure. In addition to the thermal stress caused by the temperature difference, which is related to the casting process parameters, there is the excessive thermal stress originating from a large mismatch of coefficients of thermal expansion (CTEs) between the CMC and the superalloy as extensively reported for ceramic/metal joints [14,16−20], which further contributes the thermal stress in the CMC. Another issue is the harmful interfacial graphitization reactions (Ni + SiC→Ni−Si compound + C) between Ni atoms in the superalloy melt and SiC_f/SiC, a phenomenon observed in brazing of SiC-based material/Ni-based superalloy [20−23], which can be exacerbated by the high temperature melt during the casting. It is imperative to overcome these issues. In the brazes of SiC-based material and Ni-based superalloy, the metals with good plasticity, such as the Cu insert [14,16], and the metallic matrices of the fillers (Au−Cu [10−12] and Ag−Cu [14,16,24]), have been employed to relieve thermal stress, and the reinforcing phases with low CTEs, such as TiC particles [24,25], have been introduced into brazing seam to decrease CTE mismatch. Additionally, the graphitization reactions in these brazes were alleviated by adding a layered barrier i.e., Ag [21], Mo [11,23], or W [26] layer into the brazing fillers or by using the high-entropy alloy filler [13] to retard the diffusion of Ni atoms.

To address the primary issues in integral casting, it is essential to establish a suitable interlayer at the cast interface. With this objective in mind, and considering the operability during the casting and future practical application, the process of Nb coating pretreatment on the CMC followed by precision casting with K403 superalloy melt was designed and tested. Nb has a lower CTE (8.87×10^{-6} °C^{-1} [27]) between these two base materials and a high melting point (2468 °C), thus the Nb coating should withstand the high-temperature flush of the melt and exist solidly. Consequently, this coating should effectively hinder the graphitization reactions during casting, and then convert into an interlayer which should be beneficial to interfacial high-temperature resistance for the cast and the reduction of the interfacial thermal stress caused by CTE mismatch.

In an effort to easily obtain a uniform Nb coating on SiC_f/SiC parts, a convenient chemical vapor deposition (CVD) Nb approach was invented and applied, characterized by the use of a mixed powder of Nb and NH_4Cl. The experimental results showed that the CVD-Nb pretreatment achieved satisfactory effects on the CMC/K403 cast under optimized integral casting process conditions. In the present work, the microstructure of the CVD-Nb coating and its evolution during integral casting were investigated. Furthermore, the functional mechanisms of the CVD-Nb coating on the cast interface were elucidated through the fracture mechanism analysis and comparison of the

interfacial microstructures and bonding strengths between the uncoated-CMC/K403 and the coated-CMC/K403 casts.

2 Experimental

The CMC employed in this study was manufactured by means of polymer infiltration pyrolysis (PIP) and was supplied by AECC Shenyang Liming Aero-Engine Co., Ltd. The linear expansion coefficient of the CMC is about $4\times10^{-6}\,K^{-1}$; the density is 2.4 g/cm^3 and its microstructure is shown in Fig. 1, in which the dark fiber bundles of SiC can be observed. K403 Ni-based superalloy was provided by the Aeronautical Materials Research Institute, China. The K403 superalloy has a density of 8.10 g/cm^3, a melting temperature range of 1260−1338 °C, and a linear expansion coefficient of approximately $13.8\times10^{-6}\,K^{-1}$. Its nominal composition is presented in Table 1.

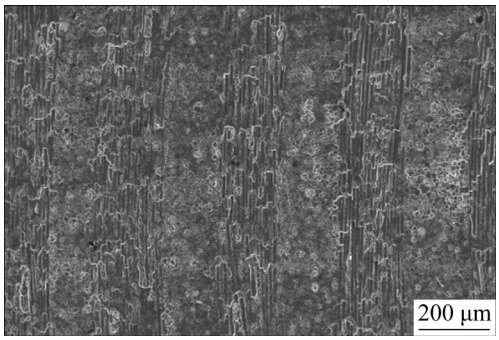

Fig. 1 Microstructure of CMC

Table 1 Chemical composition of K403 superalloy (wt.%)

C	Cr	Co	W	Mo	Al
0.16	11.05	5.26	5.16	4.20	5.60

Ti	Fe	B	Zr	Ni
2.69	0.09	0.017	0.050	Bal.

To fabricate the CVD-Nb coatings, Nb powder with 99.9% purity and a particle size of 60−80 nm, and NH_4Cl powder with 99.9% purity were used as the deposition source materials, and they were evenly mixed at a Nb/NH_4Cl mass ratio of 10:1. Prior to casting, the raw CMC was cut into 8 mm × 7 mm × 4 mm blocks, and their 4 mm × 7 mm faces, which served as the bonding surfaces, were ground with a 23 μm grade diamond abrasive tool, and then ultrasonically cleaned in acetone and fully dried at 323 K. The dried CMC blocks and the mixed powder were inserted into quartz glass tubes, which were then evacuated to a pressure of 1.0×10^{-3} Pa and immediately sealed by fusing the end glass through flame. The sealed tubes were placed into a box-type resistance furnace, heated from room temperature at a rate of 15 K/min to 1273 K, held for 300 min, and cooled down with the furnace.

To produce the CMC/K403 integrated casts, CMC blocks with or without CVD-Nb coating were assembled in a specially made Al_2O_3 ceramic mold as illustrated in Fig. 2. Within the mold, the 4 mm × 7 mm surfaces of the CMC blocks were positioned to contact the end faces of 15 mm diameter superalloy melt cylinders. Melting of the superalloy and subsequent pouring were carried out in a vacuum induction electric furnace with a vacuum degree better than 0.65 Pa. The preheating temperature for the mold and the pouring temperature for the melt were set to be 1123 and 1623 K, respectively.

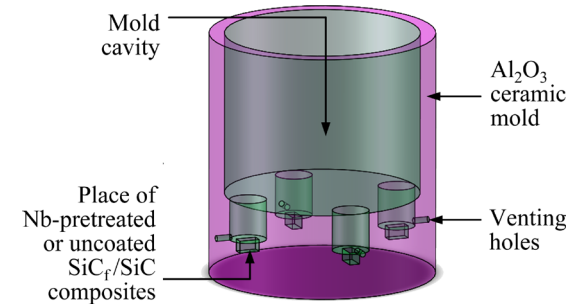

Fig. 2 Assembly diagram of CMC in Al_2O_3 ceramic mold

The cross-sectional specimens of CVD-Nb pretreated CMC blocks and the integrated casts were prepared by cutting, embedding in bakelite powder, grinding with graded diamond papers down to 5.2 μm and polishing with 0.5 μm diamond paste. All the specimens were then ultrasonically cleaned in acetone for 15 min to remove surface impurities and grease and fully dried at 323 K. The microstructures and chemical compositions for the specimens were detected using a LEO−1450 scanning electron microscope (SEM) equipped with an energy dispersive spectroscope (EDS, NORAN SYSTEM 7) and a Zeiss Auriga field emission scanning electron microscope (FE-SEM). The phases in the coating and the bonding interfaces were further identified by X-ray diffraction (XRD) using Cu K_α radiation (λ=1.5418 Å). The samples for shear test were cut from the casts and machined

in the light of the section shape shown in Fig. 3 with a superalloy thickness of 5 mm. They were then tested on a universal testing machine at a loading rate of 0.5 mm/min. The value of shear strength was obtained via dividing the shear force by the bonding area. The interface bonding strength of the cast was evaluated through averaging the shear strengths of three samples. In addition, the shear fracture morphologies were analyzed by an LEO−1450 scanning electron microscope.

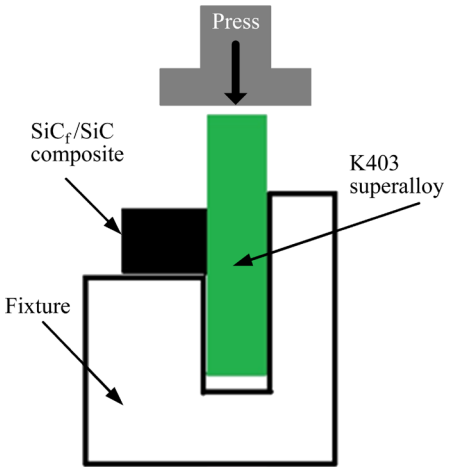

Fig. 3 Schematic diagram of shear test of integrated casting sample

3 Results and discussion

3.1 Microstructure and formation mechanism of CVD-Nb reactive coating on SiC_f/SiC composite

The formation for CVD-Nb coating prepared using a mixture of Nb and NH_4Cl powders can be elucidated through Reactions (1) and (2). According to the ΔG_T^{Θ} (change of Gibbs free energy for 1 mol atoms of reactants) expression related to temperature for Reaction (1), which was obtained by fitting the relationship between the ΔG_T^{Θ} values calculated based on thermodynamic data at different temperatures from 400 to 1400 K in Ref. [28] and the temperatures, NH_4Cl powder started to decompose and HCl gas was generated at 584.8 K during the heating process. The HCl gas then reacted with Nb powder to produce $NbCl_5$ and H_2 gases, as described in Reaction (2), whose ΔG_T^{Θ} expression was obtained through the same course as above. As the temperature increased, the ΔG_T^{Θ} for Reaction (1) became more negative, implying the generation of more HCl, which in turn reacted with Nb powder to produce more $NbCl_5$ gas. But the ΔG_T^{Θ} for Reaction (2) grew less negative with temperature increasing and turned into a positive value (184 J/mol) at the deposition temperature of 1273 K, which indicated that Reaction (2) proceeded in the opposite direction and Nb deposition occurred. This deposition reaction is in agreement with the descriptions reported in previous studies [27,29,30], where $NbCl_5$ gas (produced by Nb powder and Cl_2 gas) and H_2 were used.

$$2NH_4Cl=2HCl\uparrow+N_2\uparrow+3H_2\uparrow,\quad \Delta G_T^{\Theta}=36289-62.058T \tag{1}$$

$$10HCl+2Nb\rightleftharpoons 2NbCl_5\uparrow+5H_2\uparrow,\quad \Delta G_T^{\Theta}=-22124+17.524T \tag{2}$$

Figures 4(a−d) show the overall morphology and corresponding elemental distributions of the coating on the CMC. The coating, measuring 10−20 μm in thickness, exhibits trace amount of bakelite powder on its side due to specimen cracking between the coating and the embedded bakelite powder during preparation. It can be viewed from Figs. 4(b−d) that the coating had a high content C with a distribution similar to that in the CMC, Nb was apparently distributed in the coating, and Si was mainly distributed in the CMC. The backscattered electron image with different contrasts shown in Fig. 4(e) and the EDS results presented in Table 2 further reveal the uneven distribution of elements in the coating and the presence of a small amount of Si. The XRD pattern (Fig. 5) reveals the presence of SiC, NbC, Nb_2C, and Nb_5Si_3 phases in the coating. Notably, the information of SiC was likely derived from the CMC since the coating was thin and the NbC phase had the highest XRD intensity, indicating its highest content in the coating. The NbC, Nb_2C, and Nb_5Si_3 phases also appeared in CVD-Nb coating on SiC_f/SiC composite, which was specifically investigated using TEM by TIAN et al [27]. They identified that a reaction layer formed on the surface of SiC, consisting of NbC and Nb_5Si_3 phases. The Nb_5Si_3 phase appeared in fine size and was sparsely distributed between NbC grains. Additionally, there was a small amount of Nb_2C in the CVD-Nb coating. Hence, it is reasonable to speculate that the grey region (Region 2 in Fig. 4(e), Table 2) containing more C and a little Si in addition to Nb, and the white region (Region 3 in Fig. 4(e), Table 2) with Nb and less C were composed of NbC + Nb_5Si_3,

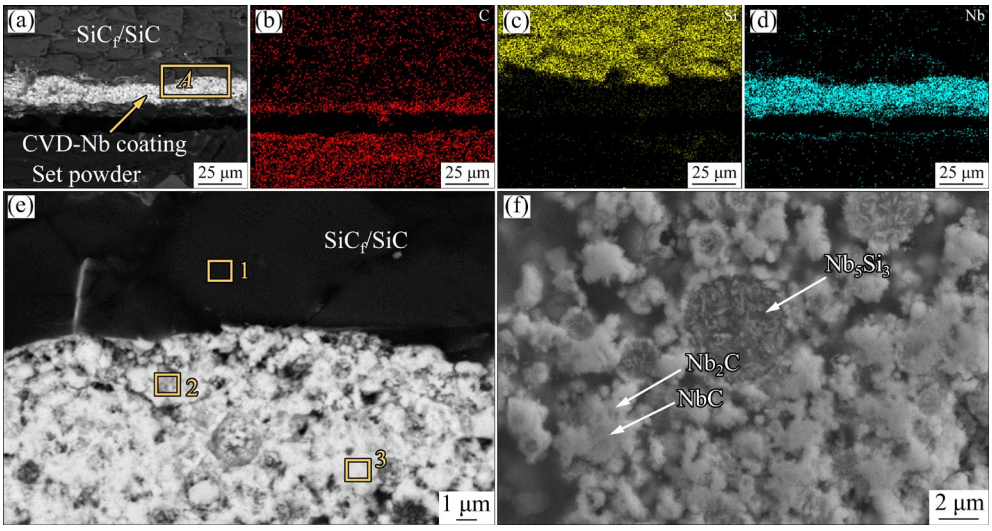

Fig. 4 Micrographs of Nb coating on CMC: (a−d) Overview cross-sectional image and elemental mappings of C, Si and Nb; (e) Magnification of Area *A* in Fig. 4(a); (f) Local magnification in Fig. 4(e)

Table 2 EDS analysis results for micro-zones marked in Fig. 4(e)

Region	Content/at.%			Possible phase
	C	Si	Nb	
1	49.11	50.69	0.20	SiC
2	50.26	3.14	46.60	NbC+Nb_5Si_3
3	45.34	−	54.66	NbC+Nb_2C

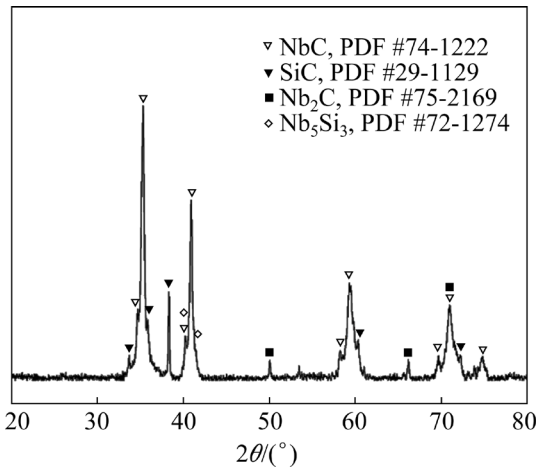

Fig. 5 XRD pattern of Nb coating on CMC

NbC + Nb_2C, respectively. These coexistence relationships also conform to the C−Nb−Si phase diagram [31]. As the grain sizes of the coating belonged to the submicron- and nano-scale, FE-SEM was used to distinguish different phases, and a secondary electron micrograph was obtained, as shown in Fig. 4(f), revealing the surface unevenness. As marked in Fig. 4(f), the white area accounting for the majority of the image was determined as NbC phase, the light gray phase corresponded to Nb_2C and the black phase denoted Nb_5Si_3 through EDS comparative analysis of the phase-included regions. Submicron- and nano-grains of NbC, and Nb_2C were also observed by TEM in the plasma spraying Nb−SiC composite powder [32].

By referring to Ref. [27], the formation of the Nb reactive coating can be described by Reactions (3), (4), (5), and (6), whose $\Delta G_T^{\ominus}$ values at 1273 K are −24.57, −68.46, −59.60, and −58.43 kJ/mol calculated on the thermodynamic data [28], respectively.

$$Nb+SiC=NbC+Si \quad (3)$$

$$Nb+C=NbC \quad (4)$$

$$2Nb+C=Nb_2C \quad (5)$$

$$5Nb+3Si=Nb_5Si_3 \quad (6)$$

On the one hand, as Nb diffused into the CMC, Reaction (3) took place, forming NbC film adjacent immediately to the CMC, which was observed using TEM [27]. On the other hand, the surface of the CMC decomposed to generate Si and C atoms, which diffused into the coating under the driving of their chemical potential gradients in Nb coating. The C atoms would diffuse more quickly owing to their much smaller atomic radius compared to that of Si atoms [27,33], resulting in the formation of NbC or Nb_2C depending on the local C content. The diffusion of the Si atoms into the coating was

hindered by the NbC film, leading to the retention of most Si atoms in CMC and the diffusion of a fewer Si atoms into the coating to form Nb_5Si_3 phase. The long reaction time in this pretreatment and the thin thickness of the Nb coating both caused the Nb coating to transform into a reactive coating with the microstructure consisting of NbC, Nb_2C, and Nb_5Si_3 phases.

3.2 Interfacial microstructure and strength of integrated cast of uncoated SiC_f/SiC and K403 superalloy

When the uncoated CMC was integrally cast with K403 superalloy melt, the resulting cast spontaneously fractured on the CMC side 1−2 mm away from the bonding interface after cooling to room temperature, as shown in Fig. 6(a), in which the upper part was residual CMC, and the lower part was K403 superalloy. The fracture location was close to the simulated maximum thermal stress site for SiC ceramics/K4169 alloy cast [15]. It could be speculated that there was a significant residual stress adjacent to the interface of the uncoated-CMC/K403 cast. The residual CMC and the areas around the interface were locally enlarged, as shown in Figs. 6(b) and (c). The element distributions in Figs. 6(d−h) demonstrate the presence of cracks and pores in the CMC near the interface. They did not incorporate the melt, which suggested that they formed after solidification of the melt and resulted from the large thermal stress during the cooling process.

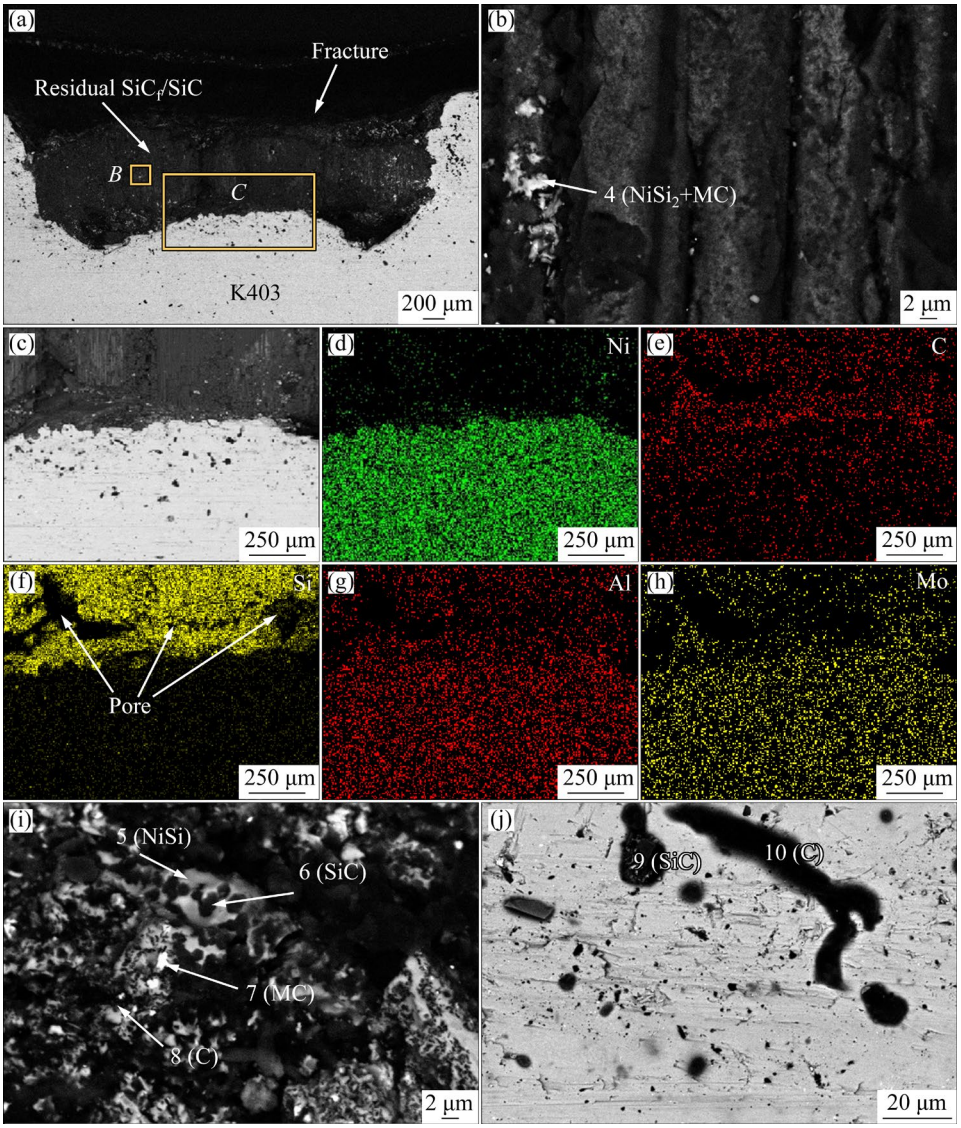

Fig. 6 Backscattered electron micrographs and sectional element distributions around interface of uncoated-CMC/K403 cast: (a) Overview; (b) Enlarged view of residual SiC_f/SiC (Area *B* in Fig. 6(a)); (c−h) High magnification images of Area *C* in Fig. 6(a) and its corresponding elemental mappings; (i) Interfacial area; (j) Enlarged view of K403 side

The microstructures at the interface and on SiC_f/SiC and K403 sides, were investigated by combining EDS spot composition analysis, phase diagrams and XRD phase structure analysis performed on the interface upon the SiC_f/SiC. The EDS composition for Region 4 in Fig. 6(b), an image of the SiC_f/SiC side away from the interface, involves two phases with different contrasts. They were identified as $NiSi_2$ (light white) and MC (M=W, Mo, Ti) (bright white) phases, according to the dominant composition (Region 4 in Fig. 6(b), Table 3) and their representation in the XRD pattern (Fig. 7), in which the TiC and MoC belong to the MC phase. The MC phase frequently occurs in K403 superalloy [34]. This indicated that elements from the melt diffused into the CMC side, leading to the graphitization reaction of Ni + SiC → Ni−Si compound + C in the C−Si−Ni system [35] and the reaction between the carbide-forming elements of Ti, Al, Mo, Cr and W from the melt and the resultant C to form the MC phase.

Owing to the high temperature, abundant reactants, and efficient channel for the diffusion and transport of elements provided by the superalloy melt, violent graphitization reaction occurred between the melt and the CMC, forming an interface reaction layer as shown in Fig. 6(i). It comprises the NiSi phase (Region 5 in Fig. 6(i)), whose dominant composition is close to the atomic ratio of NiSi phase in all the Ni−Si compounds [35,36], residual SiC particles (dark) wrapped in NiSi (Region 6 in Fig. 6(i), Table 3), MC phase (Region 7 in Fig. 6(i)), black C adjacent to Ni_2Si phase (Region 8 in Fig. 6(i), Table 3). These findings are consistent with the XRD analysis results (Fig. 7). Notably, it can be seen from Table 3 that the Ni/Si atomic ratio of the formed Ni−Si compounds changes gradually from the CMC side to the vicinity of the superalloy, presenting in the forms ($NiSi_2$→NiSi→Ni_2Si). This demonstrates existence of the mutual diffusion of the elements from the CMC and the superalloy melt to cause the concentration gradients of Ni and Si.

In the microstructure (Fig. 6(j)) of the K403 superalloy side, the granular (Region 9 in Fig. 6(j)) and irregular (Region 10 in Fig. 6(j)) black phases were identified as SiC (Region 9 in Fig. 6(j), Table 3) and C (Region 10 in Fig. 6(j), Table 3), respectively. Many of them appeared in the superalloy near the interface as shown in Fig. 6(c), suggesting that the thermal shock of the high-temperature superalloy melt produced a huge thermal stress on the SiC_f/SiC side, so that SiC particles were broken off from SiC_f/SiC and drifted into the melt. Similarly, due to the above intense interfacial graphitization reaction, a large number of C particles were generated, resulting in the drift of C particles.

3.3 Interfacial microstructure and strength of integrated cast of Nb-pretreated SiC_f/SiC and K403 superalloy

In contrast, the CVD-Nb-pretreated CMC was successfully integrally cast with K403 superalloy melt under the same above mentioned casting process, and a complete integration with no defects was obtained as shown in Fig. 8(a). The Nb-pretreated-CMC/K403 casts showed high interfacial bonding strengths with an average shear strength of 94.8 MPa (91.3, 93.8 and 99.3 MPa) at room temperature, which is higher than or roughly equivalent to the reported braze joint strengths of CMCs and Ni-based superalloys [10−13]. Figure 8(b) demonstrates a typical load versus displacement curve of the casting samples during the shear test.

Table 3 EDS analysis results for micro-zones marked in Fig. 6

Region	Content/at.%									Possible phase
	C	Si	Al	Ti	Cr	Co	Ni	Mo	W	
4	28.5	41.2	3.3	0.8	3.5	1.7	19.5	1.5	−	$NiSi_2$+MC
5	12.9	34.3	5.3	−	2.8	4.3	40.4	−	−	NiSi
6	35.4	50.9	1.0	−	2.0	1.1	9.2	0.4	−	SiC+NiSi
7	40.2	−	2.3	19.8	10.0	−	9.2	6.6	11.9	MC
8	74.9	5.8	1.7	−	2.6	1.4	13.6	−	−	C+ Ni_2Si
9	40.0	31.3	1.4	0.8	4.2	1.7	19.9	0.7	−	SiC
10	86.8	0.6	1.2	0.4	2.0	−	8.4	0.6	−	C

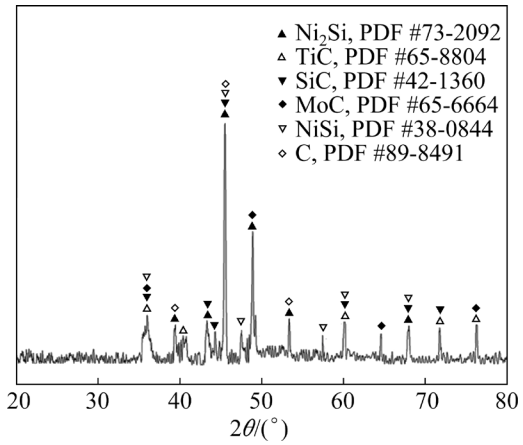

Fig. 7 XRD pattern of interface on CMC side of uncoated-CMC/K403 cast

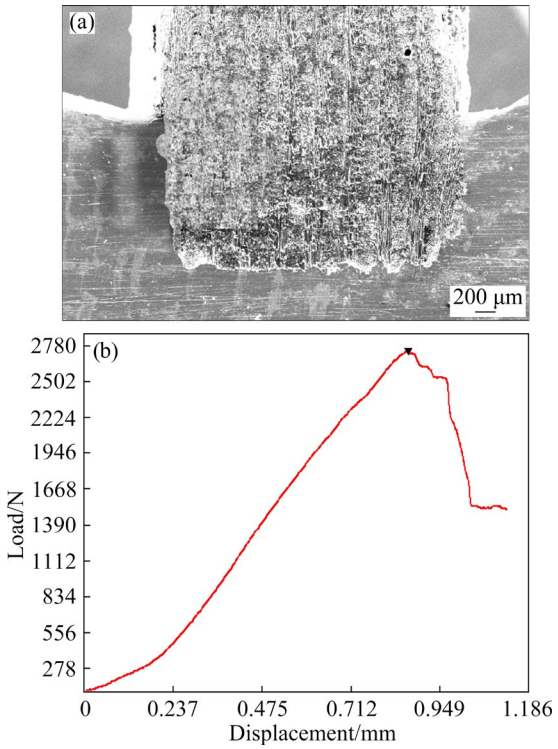

Fig. 8 Secondary electron micrograph of cross-section of Nb-pretreated-CMC/K403 cast (a) and curve of load force versus displacement of Nb-pretreated-CMC/K403 casting sample during shear test (b)

The interfacial microstructure was investigated. Figures 9(a−f) display the backscattered electron images and elemental distributions around the interface, indicating no defects such as holes and the formation of an interlayer as depicted between the two base materials. The interlayer should stem from the evolution of the Nb reactive coating. It can be observed that the Nb almost remains in place and there is the aggregation of Al from the superalloy melt, whose distribution is not entirely consistent with that of Nb and corresponds well to the black areas of the interlayer image.

To further identify the phases, the microstructures from SiC_f/SiC side (Area *D* in Fig. 9(a)) to interlayer (Area *E* in Fig. 9(a)), interlayer/K403 interface (Area *F* in Fig. 9(a)), K403 superalloy side (Area *G* in Fig. 9(a)) were magnified, as shown in Figs. 9(g−j), respectively, in which the EDS spot analyses were performed for the marked representative micro-zones with different contrasts and the results are listed in Table 4. Moreover, XRD analysis was conducted on the interlayer upon the SiC_f/SiC with the results displayed in Fig. 10.

The phase constitutions of Regions 11, 12, 13, and 15 in Fig. 9 were calibrated based on their dominant atomic compositions, the coexistence relationships outlined in the 1300 °C isothermal section phase diagram of C−Nb−Si [29], and the XRD results. Region 12 with a composition similar to that of Region 11 consists of NbC phase and $NbSi_2$ phase. The $NbSi_2$ phase (dark gray) also exists in Region 13 where the CMC (black) was originally located. Region 15 is composed of Nb_2C phase (white) and Nb_5Si_3 phase (gray). Regions 14 and 16 (black) should be of Al_4C_3 phase in accordance with their atomic compositions and only one type of aluminum carbide in the Al−C phase diagram [37]. Region 17, characterized by two different contrasts and containing a high level of Nb and small amounts of Al and Si, is likely attributable to the Nb_2Al phase (white) and Nb_5Si_3 phase (gray), which is in agreement with their presence in the XRD results of Fig. 10. Referring to the investigation of K403 superalloy [34], the bright white phase (Region 18 in Fig. 9(j)) with the composition specified in Table 4 should be of MC compound, and its surroundings consist of γ solid solution and γ' phase. The γ solid solution is the Ni-based austenite phase with multiple solute elements (e.g., Co, Cr, Mo, and W), and the dispersed γ' phase, denoted as $Ni_3(Al,Ti)$, is coherently precipitated in solid state from the γ matrix [34,38].

The absence of superalloy elements (such as Ni and Cr) on the CMC side and the lack of Nb and Si elements in the superalloy near the interlayer, as indicated by the compositions of Regions 11 and 18 in Table 4, imply that the Nb reactive coating was significantly stable under the action of superalloy

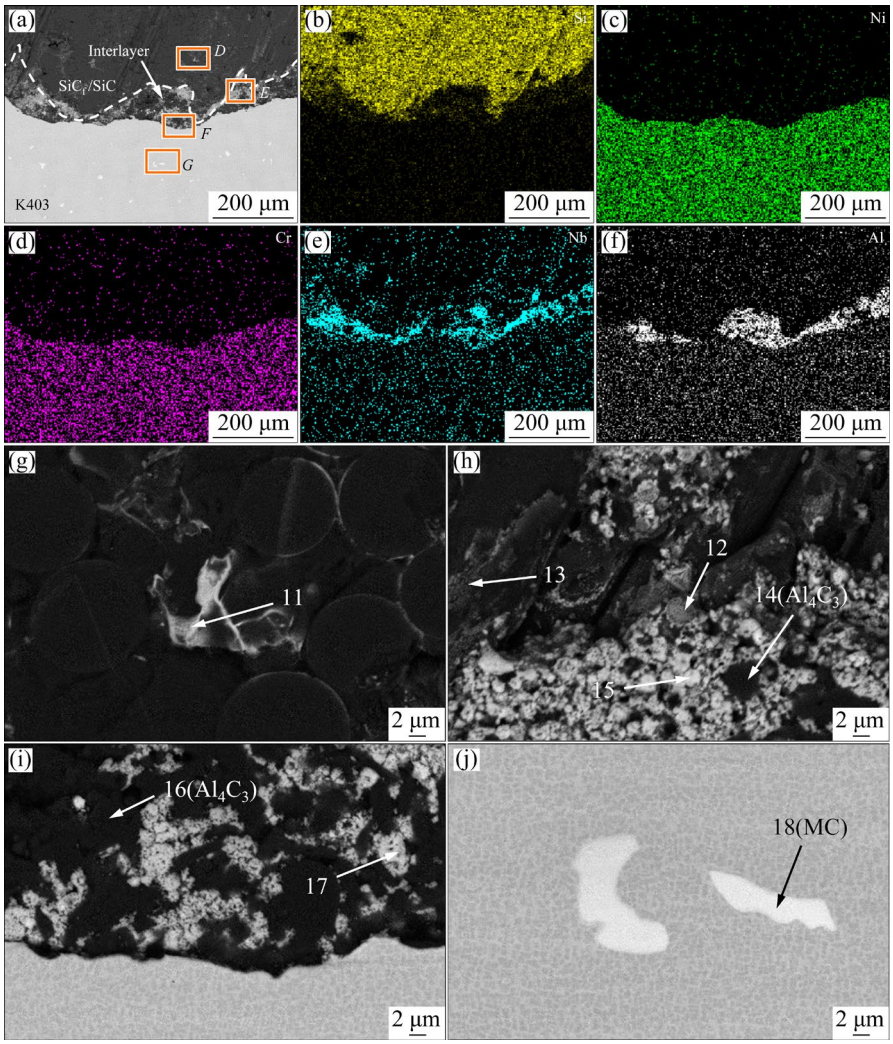

Fig. 9 Backscattered electron and sectional element distributions micrographs around interface of Nb-pretreated-CMC/K403 cast: (a−f) Overview and its corresponding elemental mappings; (g−j) High magnification images of Areas *D*, *E*, *F* and *G* in Fig. 9(a), respectively

Table 4 EDS analysis results for micro-zones marked in Fig. 9

Region	Content/at.%									Possible phase
	C	Si	Nb	Al	Cr	Ni	Ti	Mo	W	
11	23.3	39.9	36.8	–	–	–	–	–	–	NbC +$NbSi_2$
12	27.9	38.5	33.6	–	–	–	–	–	–	NbC+$NbSi_2$
13	20.6	72.7	6.7	–	–	–	–	–	–	SiC+$NbSi_2$
14	27.9	2.3	2.4	67.2	0.2	–	–	–	–	Al_4C_3
15	24.6	6.4	69.0	–	–	–	–	–	–	Nb_2C+Nb_5Si_3
16	23.7	8.1	–	68.2						Al_4C_3
17	–	7.0	83.6	9.4	–	–	–	–	–	Nb_2Al+Nb_5Si_3
18	25.3	–	–	–	3.1	6.3	45.1	10.8	9.4	MC

melt and effectively hindered the element inter-diffusion between the CMC and the superalloy, thus avoiding the graphitization reaction of Ni element and the CMC. Based on the above analysis, the change of interface microstructure from the CMC side to the K403 superalloy side can be summarized as follows: CMC, NbC, $NbSi_2$/NbC, SiC, $NbSi_2$, Nb_2C, Nb_5Si_3, Al_4C_3, Nb_2Al/γ (γ'), and MC.

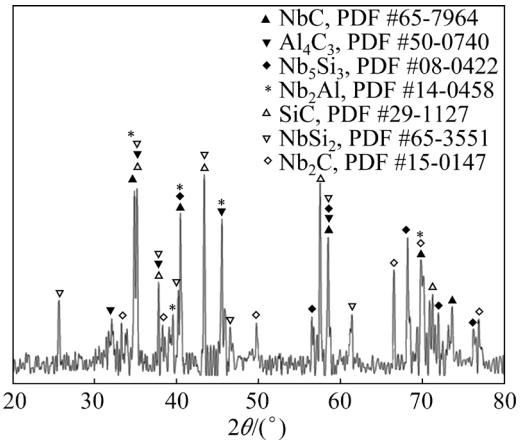

Fig. 10 XRD pattern of interlayer on CMC side of Nb-pretreated-CMC/K403 cast

Under the high-temperature condition provided by the superalloy melt, further diffusion reactions occurred, resulting in the formation of a thicker interlayer than the original coating and concentration gradients of Nb, Si and C which present as the change of compound composition (NbC, $NbSi_2$ → Nb_2C, Nb_5Si_3) from the CMC side to superalloy side interlayer (see Table 4). Due to the highest electronegativity of Al in the superalloy elements (1.61 for Al and 1.54 for Ti), which means it has the highest activity, it preferentially diffuses into the original coating during the casting as shown in Fig. 9(f). Similarly, the high activity of Al makes it able to replace some Nb in NbC as confirmed by the fact that Al can react with NbC to form $NbAl_3$ and Al_4C_3 in the temperature range from 700 to 1000 °C [39]. As Nb_2Al has a neighboring higher precipitation temperature than $NbAl_3$ among Nb−Al compounds [40], Nb_2Al is preferentially formed under the action of the high-temperature melt at 1350 °C. Comparing the microstructure of the original coating, composed of NbC, Nb_2C, and Nb_5Si_3 phases, with the microstructure of the cast interface, it can be inferred that the Al element from the superalloy melt reacted with NbC in the original coating to form $NbAl_2$, Al_4C_3, Nb_2C, and Nb phases. Nb further diffused into the CMC side under the action of high temperature and reacted with the CMC to form NbC and $NbSi_2$ phases due to the high concentrations of C and Si there, or reacted with the Si atoms previously retained near the coating to form $NbSi_2$ phase as shown in Region 13 of Fig. 9(h). Meanwhile, C and Si atoms on the CMC side diffused into the original coating, converting the pre-existing Nb_2C, Nb_5Si_3 as well as newly formed Nb_2C, Nb (residue) near the CMC into more stable NbC and $NbSi_2$ phases. In the regions of the interlayer near the superalloy, the existence of Nb and Si in the form of Nb_2C and Nb_5Si_3 is due to the lower concentration of Si and C. The C in all the Al_4C_3 phases in the interlayer should be partly derived from the CMC.

3.4 Strengthening mechanisms of integrated cast of Nb-pretreated SiC_f/SiC and K403 superalloy

Compared with the uncoated-CMC/K403 cast, the Nb-pretreated-CMC/K403 cast showed good bonding appearance and high bonding strength. This should be attributed to the reduction of thermal stress and the prevention of the interfacial graphitization reaction according to the above investigation.

In the integral casting process of the uncoated CMC and K403 superalloy melt, as the melt solidified and the temperature decreased, significant thermal stresses arose due to the shrinkage mismatch between the K403 superalloy and the CMC. Since the K403 superalloy side had a higher temperature and a larger CTE than the CMC side, it experienced correspondingly a greater shrinkage upon cooling to room temperature. According to the theory of elastic mechanics, the thermal stresses generated in the materials on both sides of the bonding interface are equal in magnitude and opposite in direction. By referencing the derivation of the thermal stress formula for a common cast [41], we derived Eq. (7) to intuitively estimate the variation trend of the interfacial stress of an integrated cast and to elucidate the effect of temperature and CTE:

$$\sigma_1 = -\sigma_2 = \frac{E_1 E_2}{E_1 + E_2}[\alpha_2 (T_2 - T_0) - \alpha_1 (T_1 - T_0)] \tag{7}$$

where σ_1, σ_2, E_1, E_2, α_1, α_2, T_1 and T_2 are stresses, elastic moduli, CTEs and bonding temperatures of the two contacted materials, respectively; T_0 is room temperature. When T_1=T_2, the formula is the usual expression of the thermal stresses for brazed joints of dissimilar materials [26]. Assuming that Material 1 and Material 2 in this formula represent the CMC and the superalloy, respectively, it can be judged that the greater the differences in temperature and CTE between the two materials are,

the greater the thermal stress is. Due to the existence of an appropriate plastic deformation on the superalloy side, the stress here was somewhat relieved, so that the maximum stress was located on the ceramic side near the interface, causing the appearance of cracks in the CMC near the interface as shown in Figs. 6(a) and (f).

In the integral casting of the Nb-pretreated CMC and K403 superalloy melt, Nb reactive coating on the surface of the CMC isolated the high-temperature melt from direct contact with the CMC. Accordingly, the temperature on the surface of the CMC and corresponding temperature gradient in the CMC would be lower compared to those of an uncoated CMC, so that a smaller thermal stress was generated inside the CMC near the interface in the cast according to Eq. (7). This could be indirectly evidenced by the fact that a large number of SiC particles drifted into the superalloy near the interface in the uncoated-CMC/K403 cast (see Figs. 6(c) and (j)), whereas this appearance did not occur in the Nb-pretreated-CMC/K403 cast (see Fig. 9(a)). When the melt was solidified, the coating fully evolved into the interlayer, which transformed the thermal stress generated by the large temperature difference between the superalloy and the CMC in the uncoated-CMC/K403 cast into the less thermal stresses generated by the smaller temperature differences between the superalloy and the interlayer and between the interlayer and the CMC in the Nb-pretreated-CMC/K403 cast, because the temperature of the interlayer must fell between the two temperatures, according to the heat transfer principle. As a consequence, the coating alleviated the thermal shock of the melt on the CMC and led to the mitigation of the interfacial thermal stress originating from temperature difference.

Because the CTE of each phase in the interlayer (SiC 4.4×10^{-6} °C^{-1} [16], Nb_3Al 6.992×10^{-6} °C^{-1} [42] , NbC 5.67×10^{-6} °C^{-1} [43], Nb_2C 6.6×10^{-6} °C^{-1} [44], $NbSi_2$ 11.7×10^{-6} °C^{-1} [45], Nb_5Si_3 $(5.04-11.86)\times10^{-6}$ °C^{-1} [46] and Al_4C_3 5.0×10^{-6} °C^{-1} [47]) falls between the CTE values of K403 (13.8×10^{-6} °C^{-1}) and CMC (4.0×10^{-6} °C^{-1}), the CTE of the interlayer (α) can be evaluated by Eq. (8) [10] and also falls between the two. Therefore, the interlayer brought about the reduction in the CTE mismatches between the superalloy and the interlayer and between the interlayer and the CMC compared with the CTE mismatch between the superalloy and the CMC, thereby lowering the thermal stress around the interface according to Eq. (7).

$$\alpha=\sum V_f\alpha_f \tag{8}$$

where α_f and V_f are the CTE and volume fraction of each phase, respectively.

Although the elastic modulus of the interlayer is estimated to be lower than that of SiC using Eq. (8) (replacing α and α_f with the corresponding E and E_f) [10], the elastic moduli (E_1 and E_2) in Eq. (7) are not sufficient to fully reflect the relationship between strain and stress, since plastic deformation is also involved during the cooling down of the cast from a high temperature. However, it is evident that the interlayer provides two strengthening mechanisms: (1) the reduction of the temperature difference and the CTE difference between two contact materials at the interface, which alleviates the interfacial thermal stress; (2) the inhibition of the interfacial graphitization reaction.

Figure 11(a) shows the SEM image of the shear fracture of the Nb-pretreated-CMC/K403 cast, displaying that the fracture occurred on the CMC side and the interlayer, and some cracks were formed in the interlayer. Therefore, it could be reasonably speculated that the crack initiated in the interlayer and propagated to the CMC during the shear loading process as depicted in Fig. 11(b). The interlayer exhibited some brittle fracture characteristics with flat surfaces and a small amount

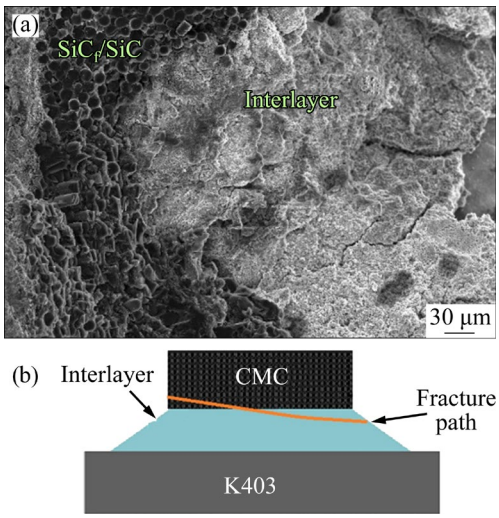

Fig. 11 Shear fracture morphology of Nb-pretreated-CMC/K403 cast (a) and fracture path diagram of cast (b)

of ductile fracture feature with steps to transfer the crack towards the CMC. In the CMC, the pull-out and interfacial debonding of SiC fibers happened, which prolonged the crack propagation and consumed the energy imposed during shearing, thereby enhancing the damage tolerance. This failure mode, which partially acted as a toughening mechanism, was consistent with the load curve variation shown in Fig. 8(b), demonstrating that the sample did not abruptly fracture with increasing load.

The Nb reactive coating effectively hindered the diffusion of Ni from the superalloy melt into the CMC, preventing the graphitization reaction during the casting process as described in Section 3.3. As a result, the strength of the CMC was not degraded, causing the fracture to originate in the interlayer rather than in the CMC near the interface as in the uncoated-CMC/k403 cast, although the maximum thermal stress occurred in this region. By optimizing the microstructure and thickness of the coating to further improve the strength and toughness of the interlayer, the shear strength for the integrated cast will be credibly elevated. This is the research direction of our subsequent study.

4 Conclusions

(1) When the CMC surface was pretreated with a mixed powder of Nb and NH_4Cl at 1000 °C, CVD-Nb occurred and underwent diffusion reaction with the CMC, forming a uniformly thick coating containing Nb carbides and Ni_5Si_3.

(2) The interface of the uncoated-CMC/K403 cast had significant thermal stress, due to the direct thermal shock of the poured superalloy melt to the CMC, as well as the large temperature difference and mismatch of CTEs around the interface in the cast. In addition, the severe graphitization reactions occurred between the Ni element from the melt and the CMC, further weakening the interface. These resulted in the formation of cracks and holes in the CMC near the interface, and the migration of SiC and C particles into the superalloy side. Consequently, effective integration between the uncoated-CMC and K403 superalloy could not be achieved through integral casting.

(3) The Nb reactive coating on the CMC effectively inhibited the diffusion of Ni element from the superalloy melt into the CMC, thereby preventing the occurrence of the graphitization reactions during integral casting. Additionally, its existence alleviated the direct thermal shock and thermal stress induced by the high-temperature melt on the CMC. As the Nb reactive coating evolved into the interlayer, the mismatches of CTEs and the temperature differences around the bonding interface were lowered, consequently reducing the thermal stress in the CMC.

(4) The average shear strength of the Nb-pretreated-CMC/K403 casts reached 94.8 MPa at room temperature, and their fractures occurred in the interlayer and its adjacent CMC during the shear test.

(5) A formula reflecting the interfacial thermal stress of an integrated cast was derived.

CRediT authorship contribution statement

Guo-biao LIN: Methodology, Writing – Original draft, Writing – Review & editing, Supervision, Resources, Funding acquisition; **Fu-hu ZHU:** Investigation, Writing – Original draft; **Jing-yu LIU:** Investigation, Visualization; **Peng LIU:** Resources, Funding acquisition; **Kai-xuan CHEN:** Writing – Review & editing.

Declaration of competing interest

The authors declare that they have no known competing financial interests or personal relationships that could have appeared to influence the work reported in this paper.

Acknowledgments

The authors gratefully acknowledge the financial support from the Fundamental Research Funds for the Central Universities, China (No. FRF-GF-18-006A).

References

[1] WANG Peng-ren, LIU Feng-qi, WANG Hao, LI Hao, GOU Yan-zi. A review of third generation SiC fibers and SiC_f/SiC composites [J]. Journal of Materials Science & Technology, 2019, 35: 2743−2750.

[2] PADTURE N P. Advanced structural ceramics in aerospace propulsion [J]. Nature Materials, 2016, 15: 804−809.

[3] KATOH Y, SNEAD L L, HENAGER C H, NOZAWA T, HINOKI T, IVEKOVIĆ A, NOVAK S, VICENTE S M G D. Current status and recent research achievements in SiC/SiC composites [J]. Journal of Nuclear Materials, 2014, 455: 387−397.

[4] LI Chang, WANG Hong-lei, YANG Ya-ping, GU Quan-chao, YAN Xing-heng, ZHOU Xin-gui. Blast and tensile properties of tantalum/niobium lined SiC/SiC composite tubes for nuclear cladding [J]. Transactions of Nonferrous Metals Society of China, 2022, 32: 1961−1968.

[5] KOYANAGI T, KATOH Y, NOZAWA T, SNEAD L L, KONDO S, HENAGER C H, FERRARIS M, HINOKI T, HUANG Q. Recent progress in the development of SiC composites for nuclear fusion applications [J]. Journal of Nuclear Materials, 2018, 511: 544−555.

[6] KIMMEL J, MIRIYALA N, PRICE J, MORE K, TORTORELLI P, EATON H, LINSEY G, SUN E. Evaluation of CFCC liners with EBC after field testing in a gas turbine [J]. Journal of the European Ceramic Society, 2002, 22: 2769−2775.

[7] VENKAT V, JUN S, DAVID J, SCOTT O, LOLA O, THOMAS L, KEVIN G, LISA P, JEFFERY S, GARY L G Z. Ceramic matrix composite turbine vanes for gas turbine engines [C]//Proceedings of the ASME Turbo Expo. Reno, Nevada: ASMEDC, 2005: 247−251.

[8] CHEN Xu, YANG Qiang, QU Lin-feng, WANG Ying-xin, WANG Fu, LI Di-chen. Stress-concentration reduction and mechanical performance improvement of C_f/SiC composite-to-superalloy joints by using topology optimization [J]. Materials & Design, 2022, 216: 110537.

[9] BA Jin, LI Pei-xin, WANG Bin, LIN Jing-huang, CAO Jian, QI Jun-lei. A novel brush surface structure of SiC_f/SiC composites designed for brazing improvement [J]. Vacuum, 2022, 195: 110700.

[10] YANG Jia, ZHANG Xun-ye, MA Guang-lu, LIN Pan-pan, XU Yan-qiang, LIN Tie-song, HE Peng, LONG Wei-min, LI Jian. Microstructural evolution and mechanical property of a SiC_f/SiC composite/Ni-based superalloy joint brazed with an Au−Cu−Ti filler [J]. Journal of the European Ceramic Society, 2021, 41: 2312−2322.

[11] YANG Jia, ZHANG Xun-ye, MA Guang-lu, LIN Pan-pan, XU Yan-qiang, LIN Tie-song, HE Peng, LIU Zhan-guo, LONG Wei-min, LI Jian. Microstructural control and reinforcement mechanism of the Mo and B inserts in the SiC_f/SiC composites/Ni-based superalloy joint [J]. Journal of the European Ceramic Society, 2021, 41: 4025−4036.

[12] ZHANG Xun-ye, LIN Jin-cheng, WANG Wei, YU Di, MA Guang-lu, LIN Tie-song, LIN Pan-pan, HE Peng, ZHAO Jia-qi. Directly construct a gradient brazed joint of SiC_f−SiC and Ni-based superalloy using a high-temperature AuCuV filler [J]. Materials Science and Engineering: A, 2022, 836: 142722.

[13] ZHAO Shuai, CHEN Hai-yan, NAI Xin, WANG Peng, DENG Huai, WEN Guo-dong, LIU Fen-jun, LI Wen-ya. Effect of Ti content on microstructure and mechanical properties of SiC_f/SiC composites/GH536 superalloy joints brazed with CoFeCrNiCuTi high entropy filler [J]. Journal of Manufacturing Processes, 2023, 85: 132−140.

[14] ZHANG Yu, GUO Wei, JIA Qiang, ZHANG Bao-liang, ZHU Ying, ZHANG Hong-qiang. Long-lasting action mechanism of 3D skeleton regulated the residual stress fluctuations in SiC_f/SiC heterogeneous joints [J]. Materials Characterization, 2023, 200: 112922.

[15] GONG Hao, ZOU Chun-ming, WEI Zun-jie, WANG Hong-wei, YANG Yong-ze. Numerical simulation on casting process of SiC ceramic/K4169 alloy composite casting [J]. Rare Metal Materials and Engineering, 2022, 51(7): 2475−2482. (in Chinese)

[16] WANG Wei, LUO Zhen-yuan, WANG Gang. Microstructure and mechanical properties of brazed In718/SiC joints with AgCuTi/Cu foam/AgCuTi composite filler [J]. Journal of Materials Research and Technology, 2023, 23: 4757−4765.

[17] PARK J W, MENDEZ P F, EAGAR T W. Strain energy release in ceramic-to-metal joints by ductile metal interlayers [J]. Scripta Materialia, 2005, 53: 857−861.

[18] YI Rui-xiang, CHEN Chao, SHI Chen, LI Yu-xiang, LI Hai-jun, MA Yi-bo. Research advances in residual thermal stress of ceramic/metal brazes [J]. Ceramics International, 2021, 47: 20807−20820.

[19] ZHANG Yan, CHEN Yan-kun, YU De-shui, SUN Da-qian, LI Hong-mei. A review paper on effect of the welding process of ceramics and metals [J]. Journal of Materials Research and Technology, 2020, 9(6): 16214−36.

[20] LIU Gui-wu, ZHANG Xiang-zhao, YANG Jian, QIAO Gun-jun. Recent advances in joining of SiC-based materials (monolithic SiC and SiC_f/SiC composites): Joining processes, joint strength, and interfacial behavior [J]. Journal of Advanced Ceramics, 2019, 8(1): 19−38.

[21] HATTALI M L, VALETTE S, ROPITAL F, STREMS-DOERFER G, MESRATI N, TRÉHEUX D. Study of SiC-nickel alloy bonding for high temperature applications [J]. Journal of the European Ceramic Society, 2009, 29(4): 813−819.

[22] XIONG Hua-ping, MAO Wei, XIE Yong-hui, GUO Wan-lin, LI Xiao-hong, CHENG Yao-yong. Brazing of SiC to a wrought nickel-based superalloy using CoFeNi(Si,B)CrTi filler metal [J]. Materials Letters, 2007, 61: 4662−4665.

[23] LI Wen-wen, CHEN bo, XIONG Hua-ping, ZOU Wen-jiang, REN Hai-shui. Joining of C_f/SiC composite to GH783 superalloy with NiPdPtAu-Cr filler alloy and a Mo interlayer [J]. Journal of Materials Science & Technology, 2019, 35: 2099−2106.

[24] SONG Yan-yu, LIU Duo, HU Sheng-peng, SONG Xiao-guo, LEI Yu-zhen, CAO Jian. Brazing of metallized SiC ceramic to GH99 superalloy using graphene nanoplatelets reinforced AgCuTi composite filler [J]. Ceramics International, 2019, 45: 8962−8970.

[25] WANG Wan-li, WANG Yong-lei, HUANG Ji-hua, YE Zheng, YANG Jian, CHEN Shu-hai, ZHAO Xing-ke. Reaction-composite diffusion brazing of C−SiC composite and Ni-based superalloy using mixed (Cu−Ti) + C powder as an interlayer [J]. Journal of Materials Processing Technology, 2022, 300: 117419.

[26] LI Shu-jie, ZHOU Ying, DUAN Hui-ping, QIU Jian-hui, ZHANG Yan. Joining of SiC ceramic to Ni-based superalloy with functionally gradient material fillers and a tungsten intermediate layer [J]. Journal of Materials Science, 2003, 38: 4065−4070.

[27] TIAN Min, LI Xiang, HE Neng, HU Wen-tao, WEI Yan, CAI Hong-zhong, CHEN Chun-lin, HU Chang-yi, HE Lian-long. TEM study on the morphology and interfacial structure of Nb-coated C_f/SiC composite [J]. Vacuum, 2022, 199: 110973.

[28] YEI Da-lun, HU Jian-hua. Handbook of practical inorganic thermodynamics [M]. 2nd ed. Beijing: Metallurgical Industry Press, 2002. (in Chinese)

[29] WEI Yan, ZHANG Da-wei, WANG Jun, CAI Hong-zhong, ZHANG Xu-xiang, CHEN Li, GUO Jun-mei, HU Chang-yi. Microstructure and deposition kinetics of Nb prepared by chemical vapor deposition [J]. Modern Physics Letters B, 2018, 32: 1850257.

[30] CHEN Li, WEI Yan, ZHU Shao-wu, CAI Hong-zhong,

MAO Chuan-jun, HU Chang-yi. Micro-structures and mechanical properties of Nb/Re layered composite produced by CVD [J]. Materials Science and Engineering: A, 2012, 536: 1−7.
[31] CACCIAMANI G, RIANI P. C−Nb−Si ternary phase diagram evaluation [EB/OL]. 2023−12−11. http://www.msi-eureka.com/full-html/10.12284.1.2/C-Nb-Si_Ternary_Phase_Diagram_Evaluation/.
[32] LI Wei, YANG Yong, LI Han, ZHANG Xia, WANG Yan-wei, TIAN Wei. TEM characterization and reaction mechanism of composite coating fabricated by plasma spraying Nb−SiC composite powder [J]. Ceramics International, 2023, 49: 15055−15064.
[33] NAKA M, FENG J C, SCHUSTER J C. Phase reaction and diffusion path of the SiC/Ti system [J]. Metallurgical and Materials Transactions A, 1997, 28(6): 1385−1390.
[34] LIU Jun, YANG He, SUN Zhi-chao, TANG Wen-ting. Effect of 950 °C thermal exposure on microstructures and properties of Ni-based K403 alloys [J]. Rare Metal Materials and Engineering, 2013, 42(6): 1123−1126.
[35] YUAN Xiao-ming, DING Jun-nan, HE Ju, HU Biao, DU Yong. Thermodynamic reassessment of the C−Ni−Si system using a four sublattice model for ordered/disordered FCC phases [J]. Journal of Phase Equilibria and Diffusion, 2017, 38: 807−813.
[36] TOKUNAGA T, NISHIO K, OHTANI H, HASEBE M. Thermodynamic assessment of the Ni−Si system by incorporating ab initio energetic calculations into the CALPHAD approach [J]. Calphad, 2003, 27: 161−168.
[37] WITUSIEWICZ V T, HALLSTEDT B, BONDAR A A, HECHT U, SLEPTSOV S V, VELIKANOVA T YA. Thermodynamic description of the Al−C−Ti system [J]. Journal of Alloys and Compounds, 2015, 623: 480−496.
[38] ALI I G, MASOUD K A, KAMRAN A, MAHDI R, REZA E K. Role of interlayer composition in microstructure and mechanical properties during TLP bonding of GTD-111/IN-718 superalloys [J]. Transactions of Nonferrous Metals Society of China, 2022, 32: 908−926.
[39] MONTEIRO W. Al−C−Nb ternary phase diagram evaluation [EB/OL]. 2023−12−11. http://www.msi-eureka.com/full-html/10.13495.1.9/Al−C−Nb_Ternary_Phase_aDiagram_Evaluation/.
[40] SILVA A A A P, COELHO G C, NUNES C A, FIORANI J M, DAVID N, VILASI M. Nb−Al binary system: Reevaluation of the solubility limits of the (Nb), Nb_3Al, Nb_2Al and $NbAl_3$ phases at high temperatures [J]. Materials Research, 2019, 22(5): e20190305.
[41] DAI Bin-yu, WANG Wei-wei. Liquid metal forming theory [M]. Beijing: National Defense Industry Press, 2010: 166. (in Chinese)
[42] PAPADIMITRIOU I, UTTON C, TSAKIROPOULOS P. Ab initio investigation of the Nb−Al system [J]. Computational Materials Science, 2015, 107: 116−121.
[43] KRASNENKO V, BRIK M G. First-principles calculations of hydrostatic pressure effects on the structural, elastic and thermodynamic properties of cubic monocarbides XC (X=Ti, V, Cr, Nb, Mo, Hf) [J]. Solid State Sciences, 2012, 14(10): 1431−1444.
[44] SCHEFFLER M, DERNOVSEK O, SCHWARZE D, BRESSIANI A H A, BRESSIANI J C, ACCHAR W, GREIL P. Polymer/filler derived NbC composite ceramics [J]. Journal of Materials Science, 2003, 38(24): 4925−4931.
[45] SON K H, YOON J K, HAN J H, KIM G H, DOH J M, LEE S R. Microstructure of $NbSi_2$/SiC nanocomposite coating formed on Nb substrate [J]. Journal of Alloys and Compounds, 2005, 395: 185−191.
[46] XU Wei-wei, HAN Jia-jia, WANG Cui-ping, ZHOU Yi, WANG Yi, KANG Yong-wang, WEN Bin, LIU Xing-jun, LIU Zi-kui. Temperature-dependent mechanical properties of alpha-/beta-Nb_5Si_3 phases from first-principles calculations [J]. Intermetallics, 2014, 46: 72−79.
[47] HASSANZADEH-AGHDAM M K. Micromechanics-based thermal expansion characterization of SiC nanoparticle-reinforced metal matrix nanocomposites [J]. Journal of Mechanical Engineering Science, 2019, 233(1): 190−201.

镍基高温合金熔体与 Nb 预处理 SiC_f/SiC 复合材料的一体化铸造

林国标[1]，朱付虎[1]，刘敬宇[1]，刘 鹏[2]，陈凯旋[1]

1. 北京科技大学 材料科学与工程学院，北京 100083；
2. 北京科技大学 国家材料服役安全中心，北京 100083

摘 要：提出了一种能制备 SiC_f/SiC 复合材料(CMC)与镍基高温合金(K403)一体化精密构件的实用工艺方法，包括对 CMC 在 1000 ℃进行化学气相沉积(CVD)Nb 涂层预处理，然后与 K403 高温合金熔体进行一体化精密铸造。该方法解决了两者之间铸造成形的困难，并形成了牢固的结合界面，其界面平均室温剪切强度达到 94.8 MPa。在预处理过程中，Nb 与 CMC 发生反应，形成由 NbC、Nb_2C 和 Nb_5Si_3 相组成的反应涂层组织。在随后的一体化铸造过程中，Nb 反应涂层有效地阻挡了高温合金熔体中的 Ni 元素与 CMC 的有害石墨化反应，减少了由于热膨胀系数失配和温度差所产生的界面热应力，导致界面强度增加。界面典型显微组织为 CMC、NbC、$NbSi_2$/NbC、SiC、$NbSi_2$、Nb_2C、Nb_5Si_3、Al_4C_3、Nb_2Al /γ/γ′和 MC(M=W, Mo, Ti)。推导了反映一体化铸件界面热应力的表达式。

关键词：SiC_f/SiC 复合材料；显微组织；镍基高温合金；一体化铸造；Nb 反应涂层；结合强度

(Edited by Wei-ping CHEN)